

# Natural convection along a micro-patterned vertical wall. Part 2: Validation of the macroscopic model for the case of transverse square ribs

Essam Nabil Ahmed<sup>a,\*</sup>, Alessandro Bottaro<sup>a</sup>, Giovanni Tanda<sup>b</sup>

<sup>a</sup>*DICCA, Università degli Studi di Genova, via Montallegro 1, 16145 Genova, Italy*

<sup>b</sup>*DIME, Università degli Studi di Genova, via Montallegro 1, 16145, Genova, Italy*

---

## Abstract

The macroscopic behavior of buoyancy-driven flows over isothermal, vertical rough surfaces is considered. The asymptotically *upscaled* boundary conditions derived in Part 1 are tested on the case of minute spanwise ribs of square cross-section. The accuracy levels and the applicability range of the proposed *effective* conditions to mimic the effects of surface micro-details on the natural-convection flow at different flow conditions and ribs' density are investigated. Feature-resolving numerical simulations are also conducted to build a reference database for the validation of the predictions of the homogenization-based macroscopic simulations. It is concluded that the accuracy of the model deteriorates with the increase of a parameter ( $C$ ) which represents the intensity of momentum and energy transfer by convection within the microscopic domain. This controlling parameter combines the effects of the Grashof number and the density of the ribs in a single accuracy criterion, yielding the formal validity limit of the present model. Besides validation purposes, the results presented provide an enhanced vision of the structure of the fluid motion and of the heat transfer characteristics of buoyancy-driven flows over vertical rough surfaces. In particular, the feature-resolving simulations reveal that two distinct inter-rib flow patterns may be present in conjunction with the increase of the flow inertia

---

\*Corresponding author

*Email address:* [essameldin.abdo@edu.unige.it](mailto:essameldin.abdo@edu.unige.it) (Essam Nabil Ahmed)

along the vertical direction; flow reattachment to the base surface is gradually lost and full separation eventually takes place. The consequent effect on the local Nusselt number is elucidated.

*Keywords:* natural convection, ribbed surfaces, effective boundary conditions, upscaling

---

## 1. Introduction and literature review

Thermal convection over ribbed/finned surfaces is widely encountered in engineering applications, such as cooling of electronics and telecommunication devices, air solar collectors, and gas-cooled nuclear reactors. Compared with forced convection, a system that depends on the natural-convection heat transfer regime has typically lower initial and running costs, less noise and vibrations, higher reliability, almost maintenance-free operations, and better ability for use in hostile environments under dust, moist air, etc. On the other hand, the main problem facing the designers is the low heat transfer coefficient of these systems, relative to those adopting active heat transfer mechanisms. Consequently, systems with relatively high heat loads usually depend on forced convection as the main cooling regime, and employ natural convection as a pack-up system [1]. On the contrary, for small and medium heat loads, the adequacy of free convection should be investigated as a first option before turning to more sophisticated systems [2].

Due to the ever-growing trend of miniaturization of electronic components, which goes hand in hand with the increase in power supply, higher heat generation rates per unit volume are encountered [3]. This trend has stimulated many investigations to enhance natural-convection cooling systems so that they can be effective at handling operation requirements. One intuitively appealing solution to enhance the heat transfer performance of these systems is to apply some sort of alteration or disturbance on the heated surface(s) in analogy to the well-established concept of heat transfer promotion by adding ribs/fins to sur-

25 faces exposed to forced convection [4, 5, 6]. However, studies on the effectiveness  
of adding surface alterations (ribs, interrupted fins, dimples, etc.) to vertical  
plates exposed to natural convection have not led yet to convincing guidelines,  
with some researchers reporting an improvement of up to 200% compared to the  
performance of plane vertical plates, and others who have found them useless  
30 or even of negative influence to the local and averaged heat transfer parameters  
[1]. At first glance, the findings of the previous studies may look contradictory;  
however, an in-depth analysis of the physics can provide insight into the possible  
reasons for the differences between the reported trends. In practice, complex  
and opposing effects often emerge, as outlined by Tanda [7], due to the following  
35 factors: (i) the presence of ribs may resist and partially block the buoyancy-  
driven stream, and consequently reduce the heat transfer rate (negative effect);  
(ii) the inactive flow regions upstream and downstream of each rib, where hot  
recirculating vortices are present, can deteriorate the heat transfer character-  
istics (negative effect); (iii) thermally conducting ribs represent an extra area  
40 for heat transfer (positive effect); (iv) the roughness elements may anticipate  
turbulence and trigger it at relatively low values of the Rayleigh number, so  
that heat transfer characteristics may improve (positive effect). Consequently,  
the overall effect of roughening a heated vertical surface has a non-systematic  
trend which may differ according to the shape of the roughness elements, the  
45 size and the distribution of the ribs on the surface, the Grashof number, the  
surface and the fluid thermal properties, etc. Since these conditions are not  
standard for all studies, favorable effects of the surface ribs have been reported  
by some researchers [8, 9, 10], whereas adverse impacts on the heat transfer  
performance were detected in other occasions [7, 11, 12].

50

The need to better understand the interaction between the surface mi-  
crostructure and the buoyancy-driven flow has initiated many experimental and  
numerical investigations that adopted different methodologies through which  
the usefulness and the feasibility of adding different types of protrusions to  
55 the heated surfaces have been assessed in terms of their effects on the flow

regime, the heat transfer characteristics, and the mass of the cooling modules. Examples of some surface alterations/extensions, considered in previous investigations are displayed in Figure 1, including corrugations [13, 14, 15, 16], steps [1], two-dimensional ribs [7, 12], and different arrangements of fins [17, 18, 19].

60 Various experimental techniques have been adopted for mapping the thermal field to assess the detailed heat transfer performance, including infrared thermography [20], the Mach-Zehnder holographic interferometry [1, 13, 15], and the Schlieren imaging methodology [7, 11, 21]. Two-dimensional and three-

65 be powerful tools for the acquisition of large amounts of data on thermal fields and flow regimes, particularly for complex configurations [12, 14, 16, 19].

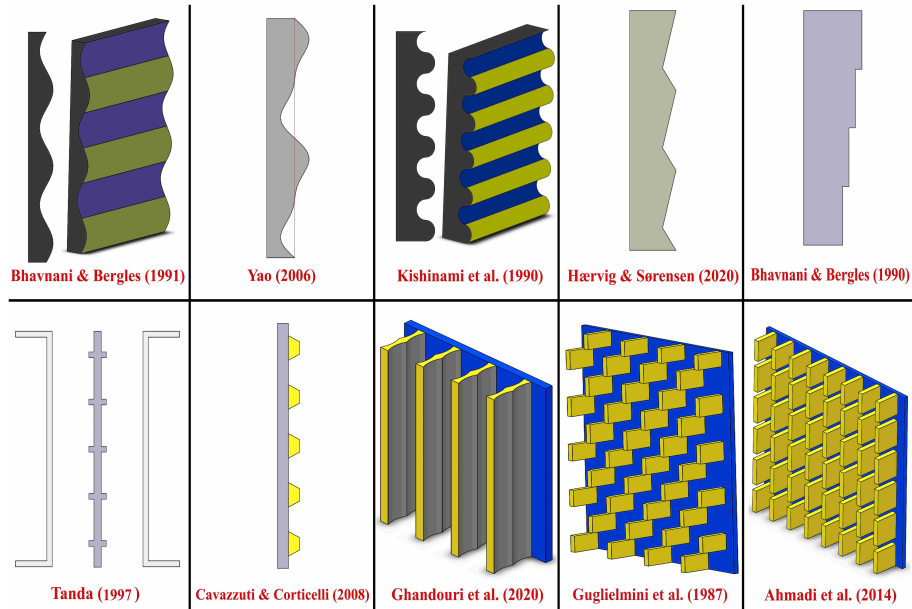


Figure 1: Schematic drawings of some surface alterations examined in the literature. The indicated geometries are (from top left to bottom right): sinusoidal waves [13], complex waves [14], convex-concave semi-circles [15], zigzag shaping [16], steps [1]; transverse square ribs [7], transverse trapezoidal ribs [12], rippled vertical fins [17], staggered arrangement of interrupted fins [18], in-line arrangement of interrupted fins [19].

Numerical work on the flows over surfaces with complicated small-scale de-

tails including irregularities, roughness, porosity, etc. has been a challenge due to the high computational resources required to numerically discretize flow and temperature fields in the vicinity of the surface microstructures. Replacing  
70 small-scale details with equivalent macroscopic effective conditions at a chosen smooth fictitious interface can considerably simplify and accelerate the computational optimization work. The asymptotic homogenization technique is a promising mathematical framework that has been recently employed for the estimation of the effective boundary conditions between a microscopic zone and  
75 the adjacent macroscopic computational domain. Even though this approach has already been adopted for the flow over rough surfaces [22, 23, 24], the heat transfer from these surfaces has not been considered yet as part of the model construction. Natural convection over rough surfaces is well suited to the homogenization approach. From the analytical perspective, the microscopic governing equations are amenable to an asymptotic expansion solution, stemming from the existence of two separate length scales, the pattern periodicity ( $\ell$ ) and the plate length ( $L \gg \ell$ ). From a numerical point of view, the need to solve the energy conservation equation, besides the momentum and the mass conservation  
80 equations, adds to the computational cost of the originally heavy fully-featured simulation. Thus, employing effective boundary conditions to avoid the full resolution of near-wall details alleviates computational requirements. Furthermore, natural convection heat transfer over perturbed surfaces is a very active field for (time-consuming) optimization studies [12, 16, 25], in order, e.g., to maximize heat transfer rate with an acceptable weight of the configuration. Using  
90 effective conditions can clearly make such studies more feasible.

This paper complements the work presented in Part 1 [26]. The asymptotic form of the effective boundary conditions that has been established in Part 1  
95 for the case of natural convection over isothermal vertical ribbed surfaces is validated in this paper for the case of the flow over a surface roughened with horizontally elongated square ribs. In the next section, the governing equations of the macroscale problem, based on the Boussinesq approximation, are set. In

Sect. 3, the basic validation case is considered with conditions that suit the  
100 adopted homogenization approach. The numerical work includes the simulation  
of the flow over a corresponding smooth surface, the feature-resolving simu-  
lation of the natural convection over the ribbed surface, and the macroscopic  
simulations with the first and second order effective boundary conditions tar-  
geted for validation. The accuracy deterioration of the proposed model away  
105 from the perfect conditions is analyzed in Sect. 4, while the validity range of  
the homogenized model is sought and formally reported in Sect. 5 which closes  
with a summary of the main conclusions of the study and the proposed plans  
to better assess the applicability of the model for its use in a variety of cases.

## 2. Problem formulation

Natural convection over an isothermal vertical surface with transverse square ribs is considered; focus is on the macroscale problem, i.e., small-scale inter-rib flow and thermal features are assumed to be irrelevant. As discussed in detail by Ahmed et al. [26], the governing equations are written with the Boussinesq approximation and normalized with suitable macroscopic scales. Eventually, the dimensionless balance equations read:

$$\frac{\partial U_i}{\partial X_i} = 0, \quad (1-a)$$

$$\frac{\partial U_i}{\partial t} + U_j \frac{\partial U_i}{\partial X_j} = -\frac{\partial P}{\partial X_i} + \frac{1}{\sqrt{Gr}} \frac{\partial^2 U_i}{\partial X_j^2} + \Theta \delta_{i1}, \quad (1-b)$$

$$Pr\sqrt{Gr} \left( \frac{\partial \Theta}{\partial t} + U_j \frac{\partial \Theta}{\partial X_j} \right) = \frac{\partial^2 \Theta}{\partial X_j^2}, \quad (1-c)$$

where the macroscopic variables are defined as:

$$U_i = \frac{\hat{u}_i}{\mathcal{U}}, \quad X_i = \frac{\hat{x}_i}{L}, \quad t = \frac{\hat{t}\mathcal{U}}{L}, \quad P = \frac{\hat{p} - \hat{p}_\infty}{\hat{\rho}_\infty \mathcal{U}^2}, \quad \Theta = \frac{\hat{T} - \hat{T}_\infty}{\hat{T}_w - \hat{T}_\infty},$$

110 using the plate height ( $L$ ), the velocity scale ( $\mathcal{U} = \frac{\nu}{L}\sqrt{Gr}$ ), the wall temperature ( $\hat{T}_w$ ) and the stagnant flow conditions (temperature:  $\hat{T}_\infty$ , pressure:  $\hat{P}_\infty$ , density:  $\hat{\rho}_\infty$ ) for normalization purposes. The fluid kinematic viscosity ( $\nu$ ) and the thermal diffusivity  $\alpha$  are constant and the Prandtl number is defined as  $Pr = \frac{\nu}{\alpha}$ . The plate Grashof number is  $Gr = \frac{g\beta(\hat{T}_w - \hat{T}_\infty)L^3}{\nu^2}$ , with  $\beta$  denoting  
 115 the constant thermal expansion coefficient.

Attention is given to validation of the expressions of the effective conditions obtained in Part 1 [26] with the upscaled coefficients calculated for the case of square ribs. Since the ribs are elongated in the transverse direction, and since  
 120 only the case of laminar flow is considered here, there is no need to resolve the spanwise direction and the problem can be simplified to its two-dimensional form in the  $(X_1, X_2)$  plane. In addition, steady-state solutions are targeted for validation purposes. Three types of simulations have been carried out: (i) natural

convection over a vertical smooth surface; (ii) full feature-resolving natural con-  
125 vection over a vertical ribbed surface; (iii) homogenized problem with effective  
boundary conditions at a virtual wall. For each simulation, the computational  
domain, the boundary conditions, and the grid structure are explained in detail  
in Sect. 3. The numerical work has been conducted using the STAR-CCM+  
multi-physics software (version 15.06.007-R8). The second-order upwind for-  
130 mulation has been adopted for the spatial discretization of all fields, with the  
calculation of the gradients based on a hybrid Gauss-least squares method. The  
SIMPLE scheme has been employed for pressure-velocity coupling.

### 3. The basic validation case

As a starting point, a typical validation case is considered; the asymptotic  
135 solution in [26] is assumed to have a reasonable accuracy provided that the  
value of the parameter  $\epsilon = \frac{\text{pattern periodicity } (\ell)}{\text{plate length } (L)}$  is sufficiently small. In addition,  
limitations are imposed on the magnitude of the coefficient of the convective  
term in the normalized microscopic governing equations,  $C = \epsilon^2 \sqrt{Gr} = \epsilon \mathcal{R}_G$ ,  
for convective effects to be absent in the leading-order problem and present at  
140 next order. For the basic validation case, we consider natural convection over an  
isothermal vertical plate with 168 transverse square ribs ( $\epsilon = \frac{1}{168}$ ) with a pitch  
distance to rib height ratio  $\frac{l}{e} = 3.75$ . The problem is characterized by a plate  
Grashof number  $Gr = 5.563 \times 10^8$  and a Prandtl number  $Pr = 0.712$ . With these  
parameters, the value of the coefficient  $C$  is 0.836. In this section a simulation  
145 of the flow over a smooth surface, at the indicated values of  $Gr$  and  $Pr$ , is first  
presented; then the feature-resolving simulations and the homogenization-based  
calculations of the ribbed surface case are considered.

#### 3.1. Isothermal vertical smooth surface case

The numerical simulation is first run on a smooth isothermal surface. Dif-  
150 ferent purposes are targeted from this step: (i) estimation of the adequacy of  
the computational domain; (ii) validation of the CFD numerical scheme and of

the inlet/outlet boundary conditions by comparing the results with available databases through the literature; (iii) the no-slip smooth surface case is equivalent to a homogenized simulation of the rough surface with zero-order effective conditions, so the results will help to monitor the effect of modelling the ribbed surface case when progressively higher-order approximations are used.

### 3.1.1. Setup of the numerical simulation

The computational domain and the boundary conditions are illustrated in Figure 2. No-slip and uniform temperature conditions are defined on the vertical wall; pressure boundary conditions are uniformly imposed at the upper and the lower boundaries such that an equilibrium with the hydrostatic pressure head is satisfied. The width of the domain should be selected in such a way that the streamwise velocity smoothly vanishes at the far boundary at  $X_2 = S$ , and the normal gradients of the horizontal velocity and the temperature smoothly go to zero. This was checked by running the simulation with different values of the domain width,  $S$ , and monitoring a result of interest (the surface-averaged Nusselt number) until convergence was attained. The local Nusselt number ( $Nu$ ) and its surface averaged counterpart ( $\overline{Nu}$ ) are defined for the smooth surface by:

$$Nu = \frac{-L}{\hat{T}_w - \hat{T}_\infty} \frac{\partial \hat{T}}{\partial \hat{x}_2} \Big|_{X_2=0} = - \frac{\partial \Theta}{\partial X_2} \Big|_{X_2=0}, \quad (2-a)$$

$$\overline{Nu} = \int_0^1 - \frac{\partial \Theta}{\partial X_2} \Big|_{X_2=0} dX_1, \quad (2-b)$$

taking into account the uniformity along the spanwise direction. As can be realized from Figure 2-b, a domain width  $S = 0.8L$  appears to be sufficient; however, a value of  $S = 2L$  was used throughout the work to ensure the absence of spurious reflections from the outer boundary when testing microstructured walls and/or larger values of  $Gr$ .

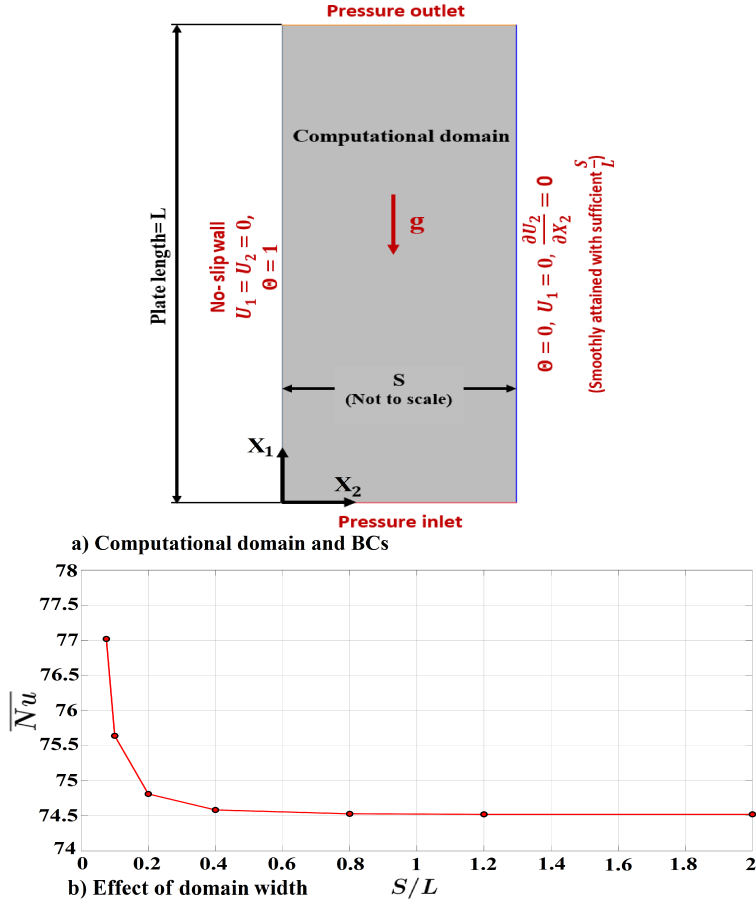


Figure 2: Computational domain with boundary conditions used for the numerical simulation of the natural convection over the isothermal vertical smooth plate ( $X_2 = 0$ ). The lower frame shows a graphical representation of the sensitivity of the solution to variations in the domain width.  $Gr = 5.563 \times 10^8$ ,  $Pr = 0.712$ .

The two-dimensional grid structure is shown in Figure 3. Special care is devoted to the domain discretization near the wall. A *near-wall layer* is thus defined to include the viscous and the thermal boundary layers where the  $X_2$ -gradients of velocity and temperature are significant. A rough estimate of the thickness of the boundary layer may be obtained based on the classical Squire-Eckert theoretical prediction [27]. Accordingly, the thickness of the boundary layers  $\delta$  (assuming  $\delta_{thermal} \approx \delta_{viscous}$ ) can be calculated based on the vertical

location along the plate ( $x_1$ ) and the local Grashof number ( $Gr_x$ ) as follows:

$$\delta = 3.936 \hat{x}_1 \left[ \frac{0.952 + Pr}{Gr_x Pr^2} \right]^{0.25}. \quad (3)$$

The maximum boundary layer thickness is reached at the end of the plate, with  $\hat{x}_1 = L$  and  $Gr_x = Gr = 5.563 \times 10^8$ . From Eq. (3), the maximum boundary layer thickness is about  $0.034L$ . As shown in Figure 3-a, the thickness of the near-wall layer for the most refined mesh is taken equal to  $0.06L$ .

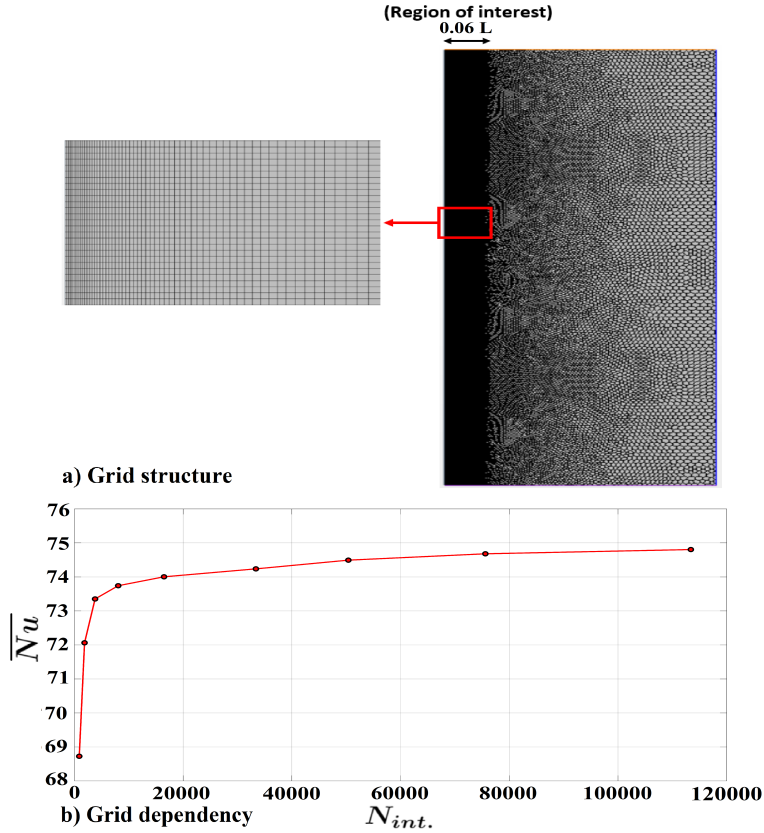


Figure 3: Description of the two-dimensional grid of the smooth plate case. A graphical representation of the solution dependence on the number of cells in the vicinity of the wall,  $N_{int.}$ , is provided in frame b). Grid convergence is achieved for a number of cells in the near-wall layer above  $10^5$ .  $Gr = 5.563 \times 10^8$ ,  $Pr = 0.712$ .

A grid-dependency study is carried out by successively refining the mesh near the surface, until the results of the surface-averaged Nusselt number converge,

as shown in Figure 3-b. For all grids tested, the mesh growth rate in the  
 170 wall-normal direction is 1.02, and the maximum cell aspect ratio is kept below  
 10 by refining the streamwise and the normal directions simultaneously. The  
 reported value of the average Nusselt number is estimated to be 75.056 based  
 on Richardson’s extrapolation of the results on the two finest meshes.

### 3.1.2. Discussion of the numerical results

The most significant results are summarized below. The dimensionless tem-  
 perature and streamwise velocity profiles are plotted across chosen normal sec-  
 tions distributed along the plate, as displayed in Figure 4. The velocity and  
 the temperature contours in the vicinity of the smooth wall are also shown, to  
 highlight the development of the boundary layers. The peak of the velocity  
 profile shifts away from the wall as  $X_1$  increase, in qualitative agreement with  
 the estimate of the classical Squire-Eckert theory [27] according to which the  
 velocity peaks at almost  $\frac{1}{3}$  of the boundary layer thickness. At the same time,  
 the temperature gradient at the wall is reduced with  $X_1$ . The latter effect is  
 responsible for the decrease of the local Nusselt number ( $Nu$ ) along the plate,  
 plotted in Figure 5. The distribution of the local Nusselt number is in perfect  
 agreement with the corresponding reference results by Ostrach [28]. An analy-  
 sis of Ostrach’s results reveals that the Nusselt number ( $Nu$ ) is related to the  
 vertical position ( $X_1$ ) via the expression

$$\frac{X_1 Nu}{\left(\frac{Gr}{4} X_1^3\right)^{0.25}} = f_n(Pr). \quad (4)$$

175 At a Prandtl number of 0.712, the function  $f_n(Pr)$  is estimated to be almost  
 0.504. Therefore, Eq. (4) can be recast as an explicit relation between  $Nu$  and  
 $X_1$  at any fixed value of the Grashof number.

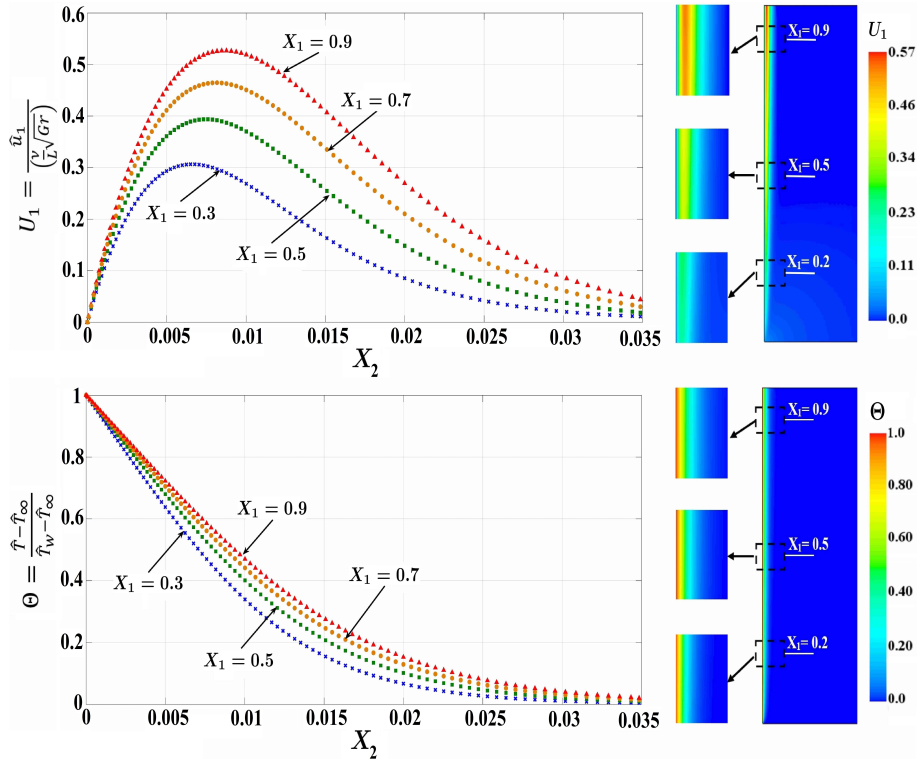


Figure 4: Smooth surface case: dimensionless velocity and temperature profiles across different normal sections along the vertical plate. Contours representing the velocity and the thermal field are also provided.  $Gr = 5.563 \times 10^8$ ,  $Pr = 0.712$ .

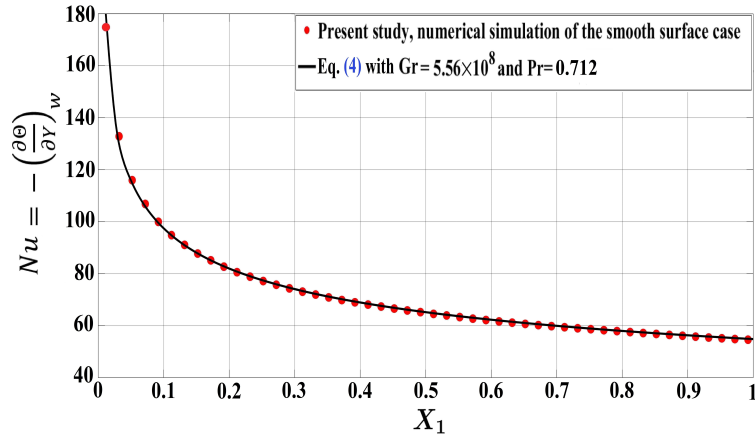


Figure 5: Smooth surface case: numerical prediction of the local Nusselt number distribution along the vertical plate, compared with the expected behavior based on the similarity solution by Ostrach [28].

The similarity solution by Ostrach [28] provides a valuable database for the validation of the velocity and the temperature fields. According to Ostrach's model, the dimensionless streamwise velocity,  $U_1^{Ost} = \frac{\hat{u}_1}{\frac{\nu}{\hat{x}_1} \sqrt{Gr_x}}$ , and the dimensionless temperature,  $\Theta = \frac{\hat{T} - \hat{T}_\infty}{\hat{T}_w - \hat{T}_\infty}$ , are functions of a similarity parameter,  $\eta = \left(\frac{Gr_x}{4}\right)^{\frac{1}{4}} \frac{X_2}{X_1}$ , for a given Prandtl number. A comparison between the present numerical results at different sections along the plate and the similarity solution is presented in Figure 6.

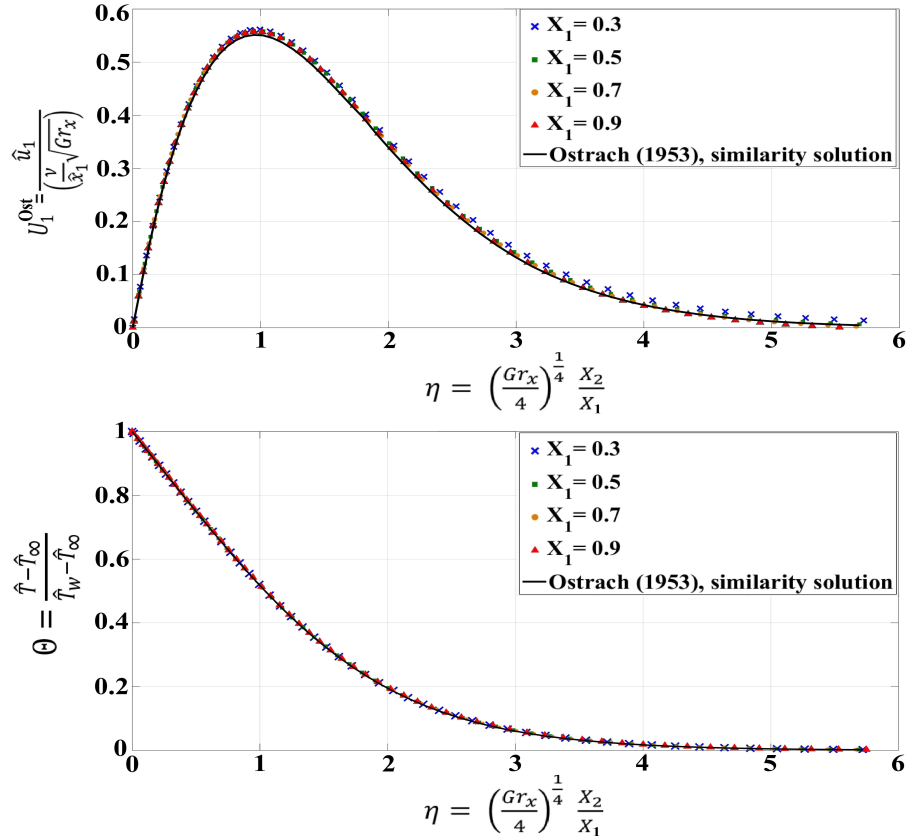


Figure 6: Smooth surface case: validation of the results of velocity and thermal fields with the reference similarity solution by Ostrach [28] at  $Pr = 0.712$ .

It is noticeable that the present results for both the velocity and the thermal fields are in good agreement with Ostrach's, especially at relatively low values of

$\eta$ , i.e., close to the wall. A similar conclusion was drawn when Ostrach compared the results of his model to experimental data from the literature, finding that the agreement was not perfect near the outer edge of the boundary layer. The slight deviation between the present results and Ostrach's solution away from the wall may be attributed to the fact that, unlike the present numerical setup, Ostrach's model considered a domain of infinite width, for the fields far from the plate to be unperturbed.

### *3.2. Feature-resolving simulation of the ribbed surface case*

The two-dimensional feature-resolving numerical simulation, where the details of the ribbed surface are captured by the grid, represents a necessary step for the validation of the homogenized model. The grid requirements and the basic results of the fully-featured simulation are discussed below.

#### *3.2.1. Setup of the simulation*

The computational domain is illustrated in Figure 7, including the geometric details of the ribbed surface. The applied boundary conditions are the same as in the smooth surface case, taking into account that the no-slip velocity and temperature conditions are now imposed on a patterned surface, not on a plain one. The two-dimensional grid near the ribs is also shown, and the different grid refinement levels are stated. A near-wall region of thickness  $5e$  is defined where a high mesh density is employed to capture the flow dynamics in the vicinity of the perturbed surface; however, the gradual growth of the mesh guarantees that the whole field is fairly well resolved. The number of two-dimensional cells given in the figure illustrate clearly the high computational cost of the fully-featured simulation of the ribbed surface compared to the smooth surface case.

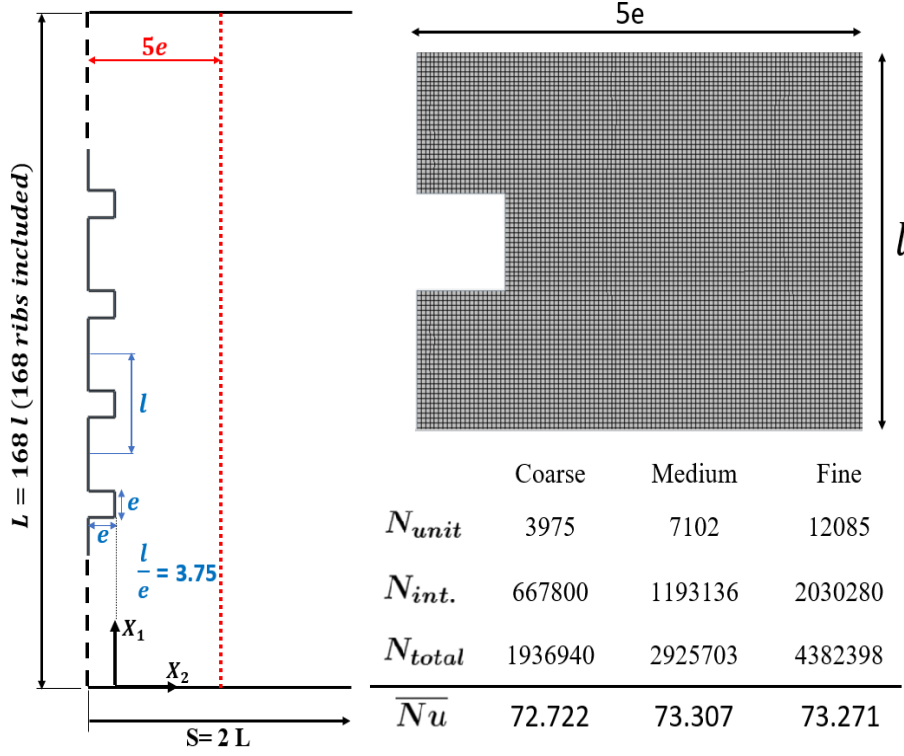


Figure 7: Description of the computational domain and two-dimensional grid structure used for the feature-resolving numerical simulation. The grid is shown for one unit in the near-wall region (of thickness  $5e$ ), defined for the highest mesh density. Indicated mesh parameters for different refinement levels are:  $N_{unit}$ : number of cells for a single unit in the near-wall region;  $N_{int.}$ : number of cells in the whole near-wall region of thickness  $5e$ ;  $N_{total}$ : total number of cells in the computational domain.

The Nusselt number at any point on the ribbed surface is given by:

$$Nu = \frac{-L}{\hat{T}_w - \hat{T}_\infty} \times \frac{\partial \hat{T}}{\partial \hat{n}} \Big|_{wall} = - \frac{\partial \Theta}{\partial n} \Big|_{wall}, \quad (5-a)$$

where  $\hat{n}$  denotes the dimensional distance in the surface-normal direction and  $n = \frac{\hat{n}}{L}$ . A dimensional surface distance  $\hat{s}$  is defined in such a way that it goes along the ribbed surface capturing its details, i.e.,  $\hat{s}$  goes from 0 to  $L + (2e \times N_{ribs})$  with  $N_{ribs} = \frac{1}{\epsilon} = \frac{L}{\ell}$  the number of ribs. Accordingly, the surface-averaged Nusselt number based on the projected area of the two-dimensional ribbed plate is

defined as:

$$\overline{Nu} = \frac{1}{L} \int_0^{L+\frac{2e}{\ell}} -\frac{\partial\Theta}{\partial n}\Big|_{wall} d\hat{s} = \int_0^{1+\frac{2e}{\ell}} -\frac{\partial\Theta}{\partial n}\Big|_{wall} ds, \quad (5-b)$$

where  $s = \frac{\hat{s}}{L}$ , and the value of  $\frac{e}{\ell}$  represents the rib height to the pitch distance ratio. The given expression for  $\overline{Nu}$  takes into account the surface area increase, with respect to the base plate area, due to the presence of ribs. The reported value of  $\overline{Nu}$  was estimated based on the Richardson's extrapolation of the available results at the successively refined meshes, and finally found to be 73.2041.

### 3.2.2. Discussion of the numerical results

The numerical results of the fully-featured simulation are described here in such a way that a vision of the associated phenomena is provided before turning to the homogenized model. The patterns of the streamwise velocity, the normal velocity, and the temperature are plotted over two distant regions along the plane surface tangent to the outer rims of the square ribs in order to show the behavior of the velocity and the thermal fields near the leading edge and near the top of the plate, as displayed in Figure 8. The fictitious surface at  $X_2 = 0$  was specifically chosen for the plots as it represents the plane on which the effective conditions will be imposed in the model simulations; therefore, monitoring the flow parameters along this surface is of interest. The contours of the velocity and the temperature near the wall are also shown so that details of the boundary layer can be captured. Velocity and temperature patterns are perturbed by the presence of the ribs and experience quasi-periodic behaviors along the vertical distance. By analyzing one unit of the distributions shown in the plots, it is evident that the no-slip velocity and temperature conditions are typically satisfied at the physical surface of the rib whereas deviations occur in the inter-rib fluid region. Proceeding along the vertical direction, the average levels of both the streamwise velocity and the temperature increase, which is qualitatively similar to the smooth surface case. The deflections of the streamlines, due to the flow interaction with the surface protrusions, are directly reflected in perturbation of

the normal velocity where the successive negative and positive fluctuations represent, respectively, the inward and outward normal flow through the inter-rib region.

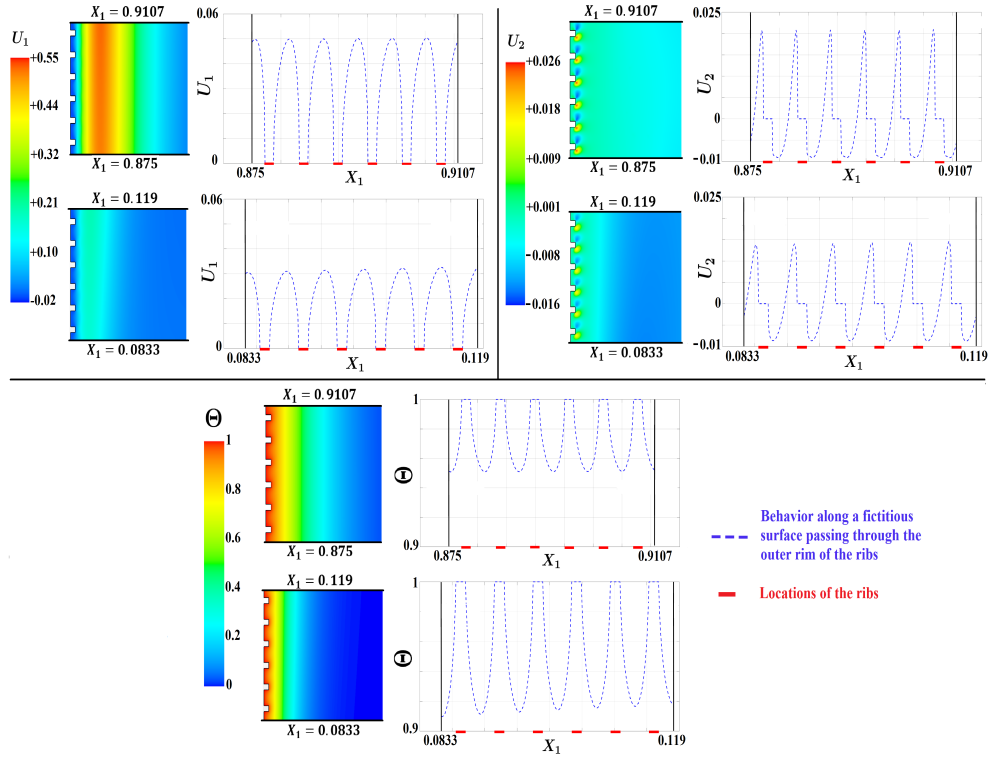


Figure 8: Feature-resolving simulation of the ribbed surface: detailed behaviors of (top left) streamwise velocity; (top right) normal velocity; (bottom) temperature. Results are plotted along the vertical plane passing through the outer rims of the ribs, through two specific ranges of  $X_1$ . The contours of the fields are also provided.  $Gr_L = 5.563 \times 10^8$ ,  $Pr = 0.712$ .

The characteristics of the flow structure and the way in which the heat transfer from the surface is accordingly affected are also analyzed, cf. Figure 9. The flow behavior close to the ribbed surface is visualized with the aid of streamlines in two distant regions along the vertical direction, so that the development of the flow can be monitored. Two distinct flow regimes are observed; namely, the *Separation-Reattachment-Separation* (SRS) regime and the *Full Separation* (FS) regime. For both patterns, the inter-rib region is characterized by the ex-

istence of two co-rotating vortices. At relatively low values of the local Grashof number  $Gr_x$ , i.e., near the leading edge, the SRS flow regime is present where  
250 the low inertia of the main stream allows the fluid to easily deflect in the normal direction and reattach to the surface of the base plate, keeping the two eddies well-isolated. In contrast, sufficiently away from the leading edge, the *Full Separation* regime takes place as the increasing inertia of the accelerated stream hinders the normal deflection towards the base plate and prevents the  
255 reattachment of the main stream. As illustrated in the figure, the two vortices remain connected to each other via an outer belt-like stream that rotates in the same direction of both eddies, representing a separated entity that isolates the main flow from the base plate in the inter-rib region.

260 The associated heat transfer behavior is plotted in Figure 9 in terms of detailed pattern of the local Nusselt number  $Nu$ . A quasi-periodic behavior of the Nusselt number is observed while proceeding along the vertical plate in a similar way to the patterns reported in the literature [1, 7, 10, 11, 21]. On a single-unit scale of analysis, it is evident that the heat transfer rate drastically  
265 drops just upstream and downstream of the square protrusion, a fact ascribed to the presence of the separation eddies that form a hot inactive zone in the vicinity of the rib where the thermal boundary layer thickening mitigates the heat transfer process. Conversely, the local Nusselt number peaks at some location within the inter-rib region as the main stream reattaches to the surface of the  
270 base plate. Even in the *Full Separation* regime, the inter-rib peak is experienced since the main stream still approaches the surface (without reattaching). The major peak of the local Nusselt number is present on the outer rim of the rib due to the considerable local thinning of the thermal boundary layer. From a macroscopic point of view, the average value of  $Nu$  decreases away from the  
275 leading edge along with the development of the thermal boundary layer.

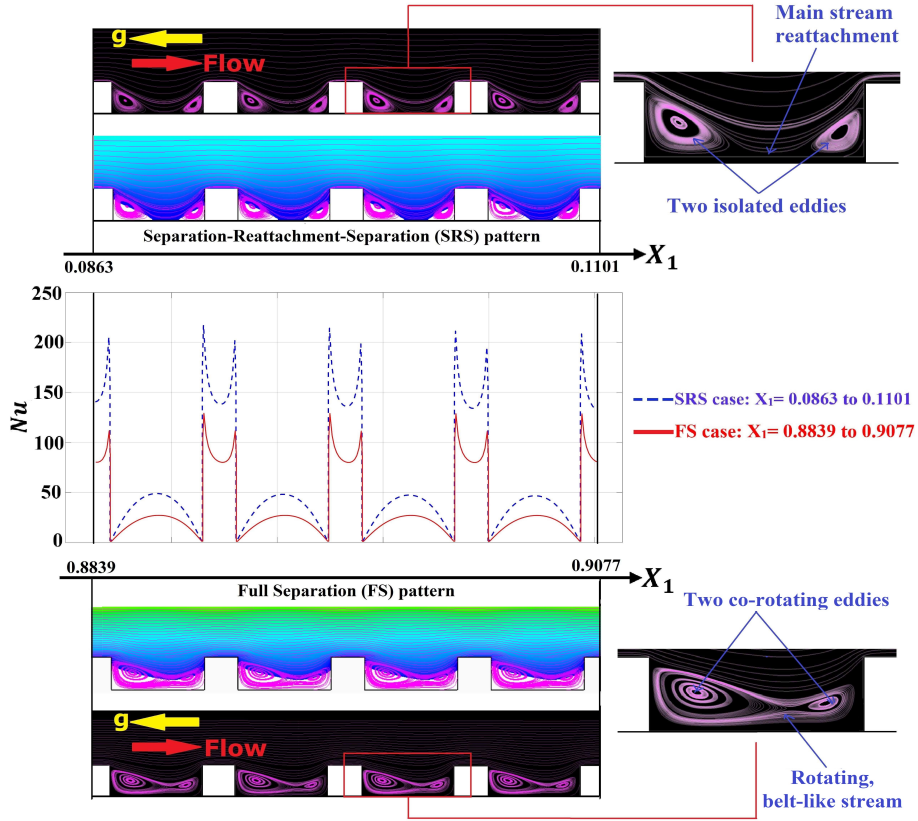


Figure 9: Feature-resolving simulation of the ribbed surface: Comparative description of the flow pattern and the behavior of the Nusselt number through two distant regions: (top) near the leading edge; (bottom) near the end of the plate. The contours of  $U_1$  are also shown; the color map given in Figure 8 is modified here so that the white portions within the grooves represent the regions with negative streamwise velocity, i.e., the back-flow regions.  $\epsilon = \frac{1}{168}$ ,  $\frac{l}{e} = 3.75$ ,  $Gr = 5.563 \times 10^8$ ,  $Pr = 0.712$ .

### 3.3. The macroscopic homogenization-based simulations

The effect of the surface microstructure on the behavior of the buoyancy-driven stream is replaced here by the implementation of the homogenized effective boundary conditions on the plane at  $X_2 = 0$  (refer to Figure 7), based on the asymptotic model that was developed in Part 1 [26]. As the present work targets the validation of the model on the steady-state solution of a two-dimensional laminar flow, the effective conditions can be simplified by neglecting the time-derivative terms and the gradients in the spanwise direction. The dimensionless

conditions up to the second order in all variables thus read:

$$U_1|_{X_2=0} = \epsilon [\lambda_x S^{12} + m_{12} \mathcal{R}_G]_{X_2=0} + \epsilon^2 \left[ m_{12} \frac{\partial S^{22}}{\partial X_1} + \mathcal{B} \mathcal{R}_G \frac{\partial \Theta}{\partial X_2} \right]_{X_2=0} + \mathcal{O}(\epsilon^3), \quad (6-a)$$

$$U_2|_{X_2=0} = -\epsilon^2 \left[ m_{12} \frac{\partial S^{12}}{\partial X_1} \right]_{X_2=0} + \mathcal{O}(\epsilon^3), \quad (6-b)$$

$$\Theta|_{X_2=0} = 1 + \epsilon \lambda_z \frac{\partial \Theta}{\partial X_2} \Big|_{X_2=0} + \mathcal{O}(\epsilon^3), \quad (6-c)$$

where the reduced Grashof number,  $\mathcal{R}_G$ , and the macroscopic dimensionless stress components,  $S^{12}$  and  $S^{22}$ , are defined as:

$$\mathcal{R}_G = \epsilon \sqrt{Gr}, \quad S^{12} = \left( \frac{\partial U_1}{\partial X_2} + \frac{\partial U_2}{\partial X_1} \right), \quad S^{22} = -P \sqrt{Gr} + 2 \frac{\partial U_2}{\partial X_2},$$

with the macroscopic dimensionless pressure  $P$  defined in Sect. 2. The model upscaled coefficients  $(\lambda_x, \lambda_z, m_{12}, \mathcal{B})$  are dependent on the rib geometry, that is, the coefficients are all functions of  $\frac{l}{e}$  for the case of the square ribs. Based on the parametric study presented in Part 1, at  $\frac{l}{e} = 3.75$ , the following values of the model coefficients are found:

$$\lambda_x = 0.03791, \quad \lambda_z = 0.08404, \quad m_{12} = 0.002125, \quad \mathcal{B} = 0.0002247. \quad (7)$$

Both the streamwise velocity and the temperature have a first-order term in  $\epsilon$ , whereas a transpiration velocity component appears only at second order. While the streamwise velocity is further corrected at second order, the term in the temperature condition vanishes at this order for a steady-state solution. Since the ribbed surface is impermeable, the transpiration velocity is zero on average and its inclusion is not significant under laminar flow conditions; this was tested and confirmed in the present work.

### 3.3.1. Setup of the homogenized simulations

The setup of the homogenization-based macroscopic simulations is similar to the setup of the smooth surface case with regard to the computational domain, the grid structure, the refinement levels and the boundary conditions except for replacing the no-slip velocity and temperature conditions by the effective

conditions (Eqs. (6)) on a virtual wall in  $X_2 = 0$ , up to second order. It is  
 290 comforting that the macroscopic simulations reach mesh-independence for grids  
 which are more than 30 times coarser as compared to the fully-featured case,  
 while providing accurate predictions of the surface-averaged Nusselt number  
 (the metric being evaluated in the grid-dependence study). The converged val-  
 ues of  $\overline{Nu}$  with first-order and second-order conditions are, respectively, 73.3380  
 295 and 73.3366. In comparison to the fully-featured result the errors of the homog-  
 enized models are, respectively, 0.183% and 0.181%. It is worth mentioning that  
 $\overline{Nu}$  of the smooth surface case is 2.5290% higher than the fully-featured ribbed  
 case; adding ribs to the vertical surface deteriorates the total heat transfer rate,  
 for the geometric parameters and flow conditions under study.

### 300 3.3.2. Validation of the homogenized fields

The results which can be achieved from the homogenized simulations rep-  
 resent the macroscopic behavior of velocity and temperature fields, while the  
 detailed perturbed patterns near the wall cannot be captured. For this purpose,  
 the validation of the present approach is done by comparing the results of the  
 macroscopic simulations with the running-average values of the fully-featured  
 fields over streamwise distances equal to the periodicity of the pattern of the  
 surface structure. For instance, the running-average value of the dimensionless  
 velocity  $U_1$  at an arbitrary point ( $X_1 = a$ ,  $X_2 = b$ ) is computed as:

$$\langle U_1 \rangle \Big|_{X_1=a, X_2=b} = \frac{1}{\epsilon} \int_{a-\frac{\epsilon}{2}}^{a+\frac{\epsilon}{2}} U_1(X_1, b) dX_1. \quad (8)$$

The numerical predictions of  $U_1$  and  $\Theta$  resulting from the macroscopic simu-  
 lations with the first-order accurate and the second-order accurate boundary  
 conditions are extracted at the fictitious boundary in  $X_2 = 0$  to explicitly as-  
 sess the accuracy of the expressions given in Eqs. (6). The homogenized results  
 305 are plotted in Figure 10 in comparison with the corresponding running-average  
 values of the feature-resolving simulation.

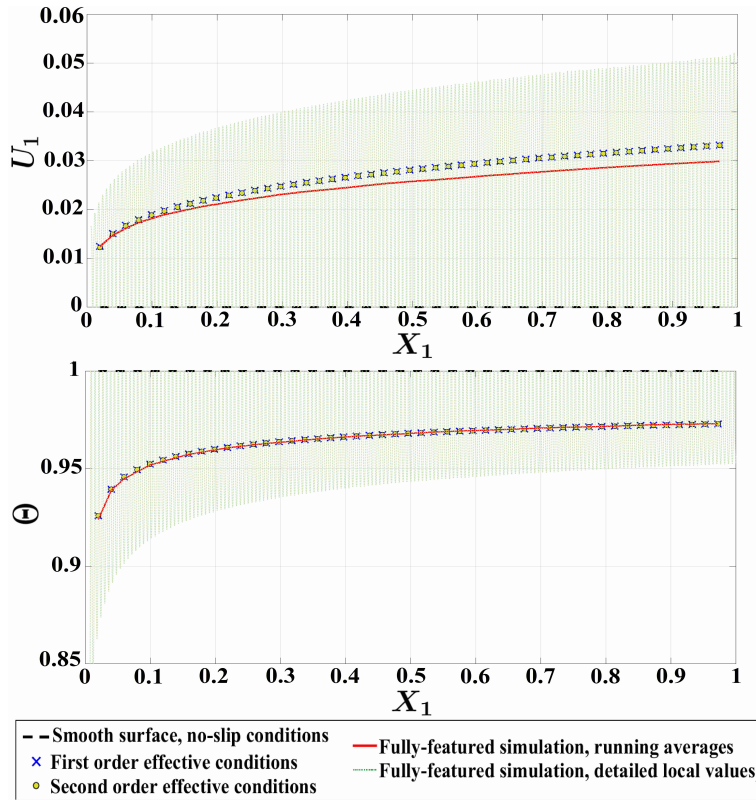


Figure 10: Effective boundary conditions for streamwise velocity and temperature in comparison to the running-average results of the feature-resolving simulation.  $\epsilon = \frac{1}{168}$ ,  $\frac{l}{e} = 3.75$ ,  $Gr = 5.563 \times 10^8$ ,  $Pr = 0.712$ .

It is clear that the present model can qualitatively predict the difference of the results from the no-slip values. The results show perfect agreement of the effective temperature estimates, apparently insensitive to the mild deviations  
 310 observed for the predictions of the slip velocity. This fact may be attributed to the absence of strong non-linearities, i.e. the coupling between the velocity and the thermal fields is weak.

In order to show how the effect of the homogenized conditions propagates  
 315 from the virtual wall to the flow domain, the profiles of streamwise velocity and temperature are plotted across two normal sections and compared with the

corresponding running-average profiles (Figures 11 and 12).

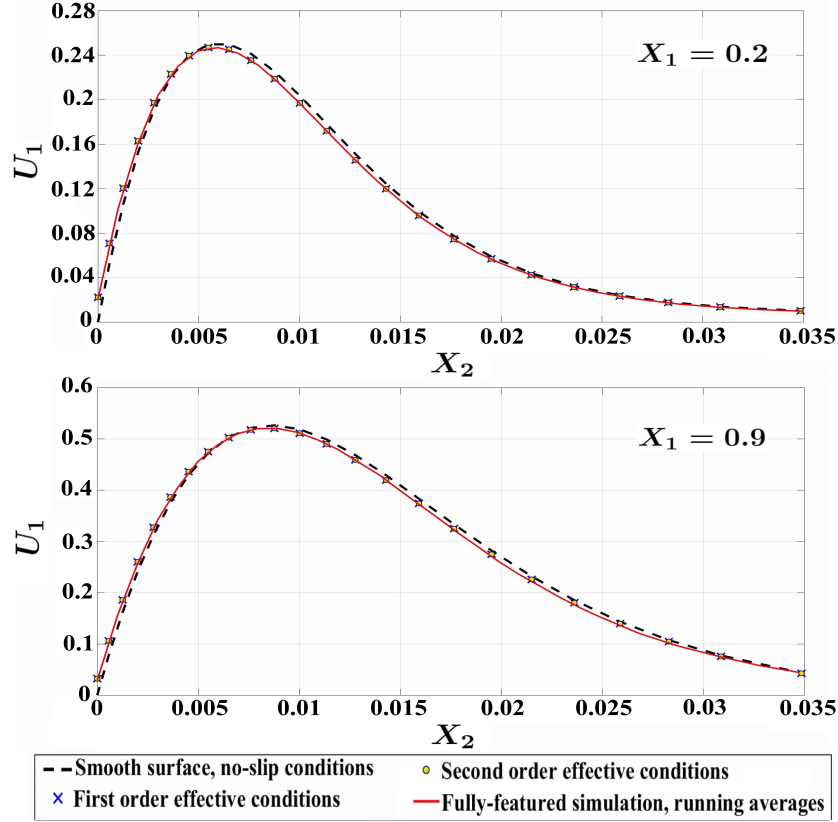


Figure 11: Homogenized-model predictions streamwise velocity profiles across two normal sections in comparison to the running-average results of the fully-featured simulation.  $\epsilon = \frac{1}{168}$ ,  $\frac{l}{e} = 3.75$ ,  $Gr = 5.563 \times 10^8$ ,  $Pr = 0.712$ .

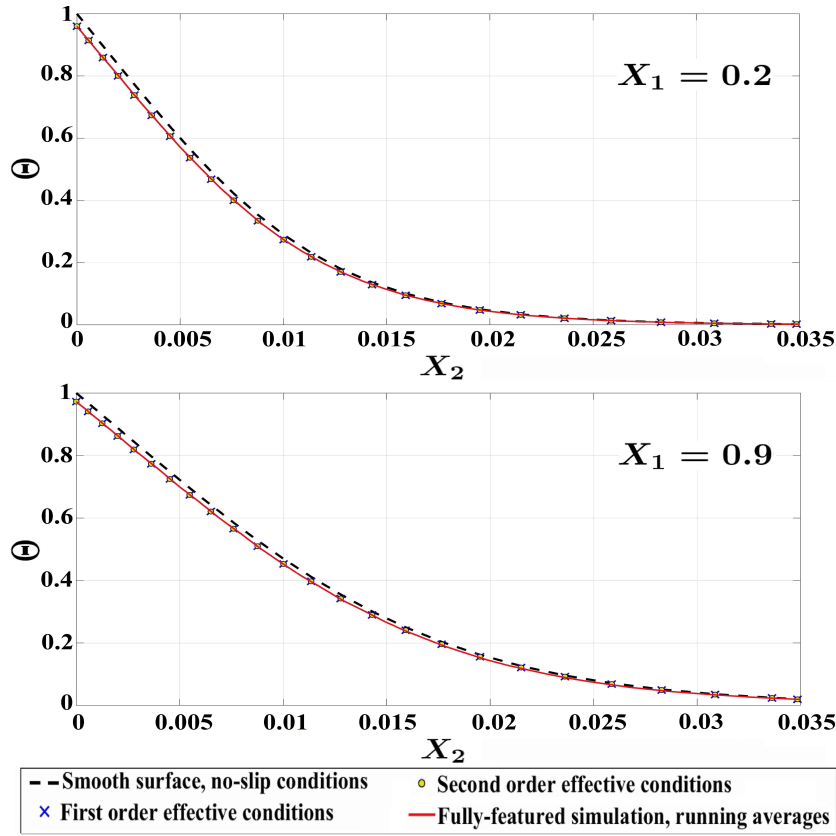


Figure 12: Validation of the homogenized-model results of the temperature profiles across two normal sections in comparison to the running-average results extracted from the fully-featured simulation.  $\epsilon = \frac{1}{168}$ ,  $\frac{l}{e} = 3.75$ ,  $Gr = 5.563 \times 10^8$ ,  $Pr = 0.712$ .

It is noticeable that, in the present case, the effect of the surface inhomogeneities on the flow field is moderate. Another point is that the predictions based on first and second-order conditions are almost indistinguishable from one another to graphical accuracy, due to the very small value of  $\epsilon$ . The normal gradients of  $\Theta$  along the fictitious boundary, represented by the slopes at  $X_2 = 0$  of the  $\Theta$  profiles, were used to obtain the macroscopic behavior of the Nusselt number along the plate (cf. Eq. (2-a)). The results are presented in comparison with the corresponding running-average values from the fully-featured simulation in Figure 13. It can be realized that, under the present conditions, the ribs on

the surface have a very mildly unfavorable effect on the heat transfer rate, as reported also in Section 3.3.1.

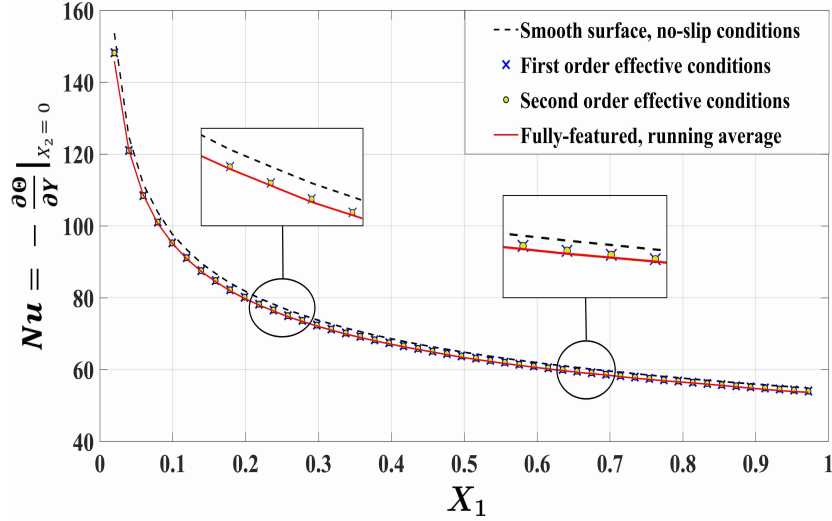


Figure 13: Homogenized model predictions of the Nusselt number in comparison to the running-average results of the feature-resolving simulation, based on the normal temperature gradient along the plane  $X_2 = 0$ .  $\epsilon = \frac{1}{168}$ ,  $\frac{l}{e} = 3.75$ ,  $Gr = 5.563 \times 10^8$ ,  $Pr = 0.712$ .

It is very important to highlight that the present approach is only able to model  
 330 the temperature-gradient-based heat transfer from the matching interface, while  
 the non-linearity of the convective part, resulting from the product of normal  
 velocity and temperature, is not accounted for, since the fluctuations of the  
 normal velocity cannot be resolved by the homogenized model under laminar  
 flow conditions. The applicability of the model is, therefore, limited here to cases  
 335 in which convective effects through the fictitious plane are negligible. This is  
 assumed to be valid in the absence of strong non-linearities that may occur for  
 large values of  $\epsilon$  or in the presence of turbulence.

#### 4. Accuracy of the homogenized model

In this section, the results of several numerical simulations are presented  
 340 to assess the deterioration of the results of the proposed technique with the

increase of the small parameter  $\epsilon = \frac{\ell}{L} = \frac{1}{N_{\text{ribs}}}$  and the coefficient of the microscopic momentum-convective term  $C = \epsilon^2 \sqrt{Gr} = \epsilon \mathcal{R}_G$ , whose effects were preliminarily discussed at the beginning of Section 3.

#### 4.1. Effects of the increase in $\epsilon$ at a given Grashof number

345 The simulations of the macroscopic problem are now conducted for increasing values of the parameter  $\epsilon$  in the effective boundary conditions (Eqs. (6)), starting from  $\epsilon = \frac{1}{84}$  up to  $\epsilon = \frac{1}{10}$ , at a constant value of the Grashof number ( $Gr = 5.563 \times 10^8$ ) and for the values of the model coefficients at  $\frac{\ell}{e} = 3.75$  (cf. Eq. (7)), in order to monitor the deterioration of the model with the increase  
350 of the controlling parameters  $\epsilon$  and  $C$ . First, a validation database has been built by running the fully-featured simulations with the corresponding numbers of ribs (from 84 to 10). The running-average fields of the different fully-featured simulations along the plane  $X_2 = 0$  and across a normal section at the middle of the plate are presented in Figure 14 in a comparative manner to get an idea  
355 about the effects of increasing  $\epsilon$  on the flow characteristics. Note that the results of the corresponding smooth surface simulation and the previously shown results of the case  $\epsilon = \frac{1}{168}$  are included in the figure.

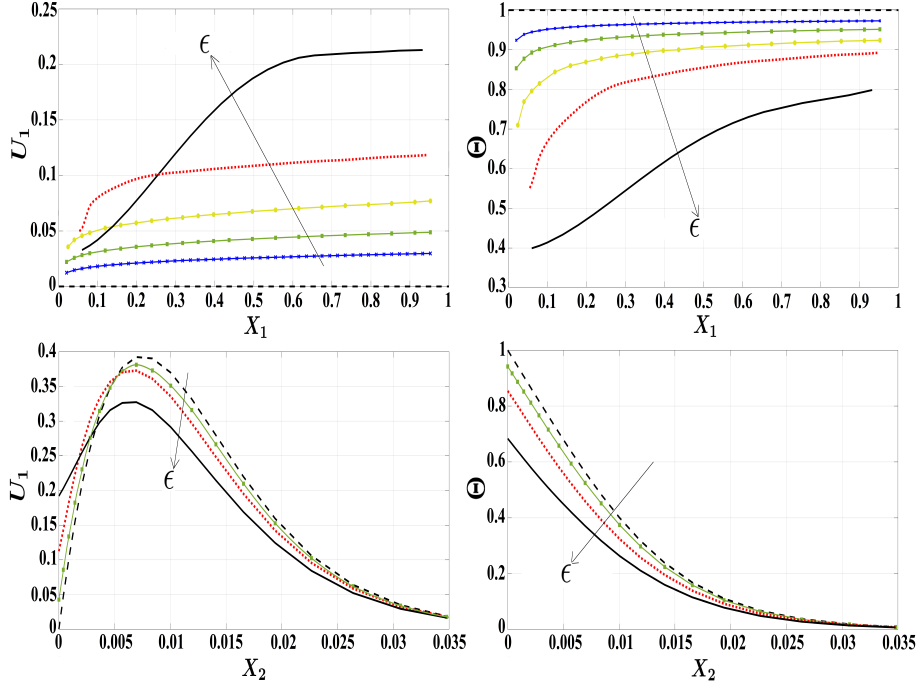


Figure 14: Fully-featured simulations with different values of  $\epsilon$ : (top) running-averaged behaviors of the dimensionless streamwise velocity (left) and temperature (right) along the plane  $X_2 = 0$ ; (bottom) running-averaged profiles of the dimensionless streamwise velocity (left) and temperature (right) across a normal section at  $X_1 = 0.5$ . Curves are: smooth surface (dashed black line),  $\epsilon = \frac{1}{168}$  (blue line),  $\epsilon = \frac{1}{84}$  (green line),  $\epsilon = \frac{1}{42}$  (yellow line),  $\epsilon = \frac{1}{21}$  (red dotted line),  $\epsilon = \frac{1}{10}$  (solid black line). For all cases,  $\frac{l}{\epsilon} = 3.75$ ,  $Gr = 5.563 \times 10^8$ ,  $Pr = 0.712$ .

The analysis of the velocity and the temperature distributions along the fictitious boundary (Figure 14-(top)) reveals that the slip velocity (deviation from  $U_1 = 0$ ) and the thermal slip (absolute deviation from  $\Theta = 1$ ) increase with  $\epsilon$ , which qualitatively agrees with the dependence given in Eq. (6). The magnitude of the normal temperature gradient at the wall decreases with  $\epsilon$ , i.e. the heat transfer from the wall is reduced. It is also observed that the temperature level away from the surface is lower as  $\epsilon$  increases, which in turn yields a reduction of the buoyancy term in the momentum equation, thus reducing the velocity peak.

The results of the macroscopic simulations with first-order and second-order accurate homogenized effective conditions are validated by comparing the

streamwise velocity profiles and the temperature profiles across a normal section  
 370 taken at  $X_1 = 0.5$  with the corresponding running-average patterns from the  
 fully-resolved numerical simulations, cf. Figures 15 and 16. The purpose is to  
 get an idea about the validity range of the asymptotic model away from the  
 conditions ( $\epsilon = \frac{1}{168}, C = 0.836$ ) discussed in Sect. 3.

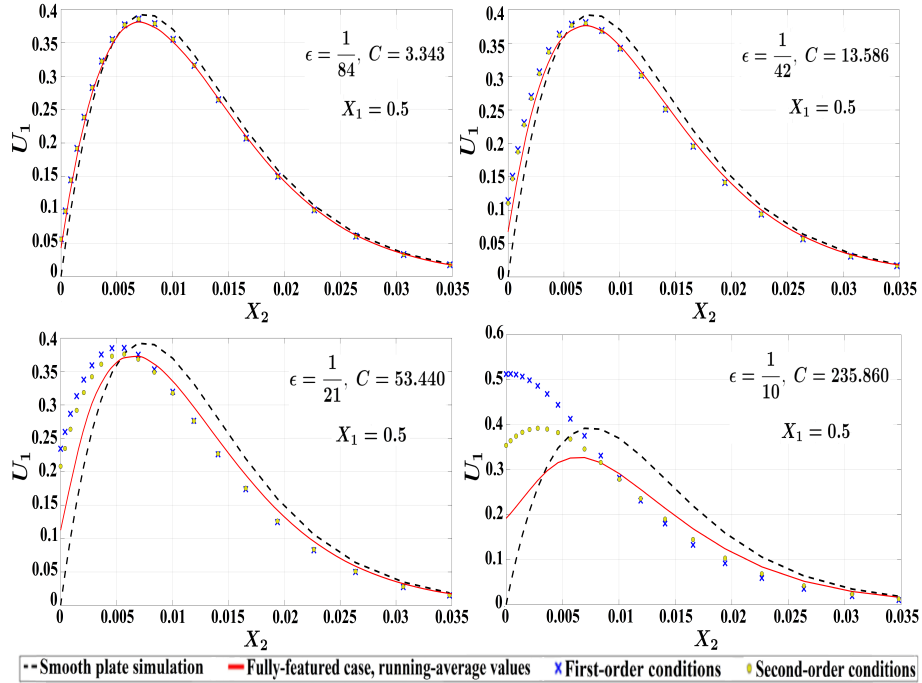


Figure 15: Predictions of the homogenized-models in comparison to the fully-featured running-average results of the dimensionless streamwise velocity profiles at  $X_1 = 0.5$  for different values of  $\epsilon$ .  $\frac{l}{c} = 3.75$ ,  $Gr = 5.563 \times 10^8$ ,  $Pr = 0.712$ .

In general, the predictions of the present approach concerning velocity and temperature fields are reliable below  $\epsilon = \frac{1}{21}$  at the given Grashof number. It will  
 375 be argued later that the reliability range becomes wider at lower values of the Grashof number. The accuracy of the temperature predictions is better than the velocity predictions, especially above the mentioned limit where the boundary conditions at second order are able to produce better results in comparison  
 380 to the first-order conditions.

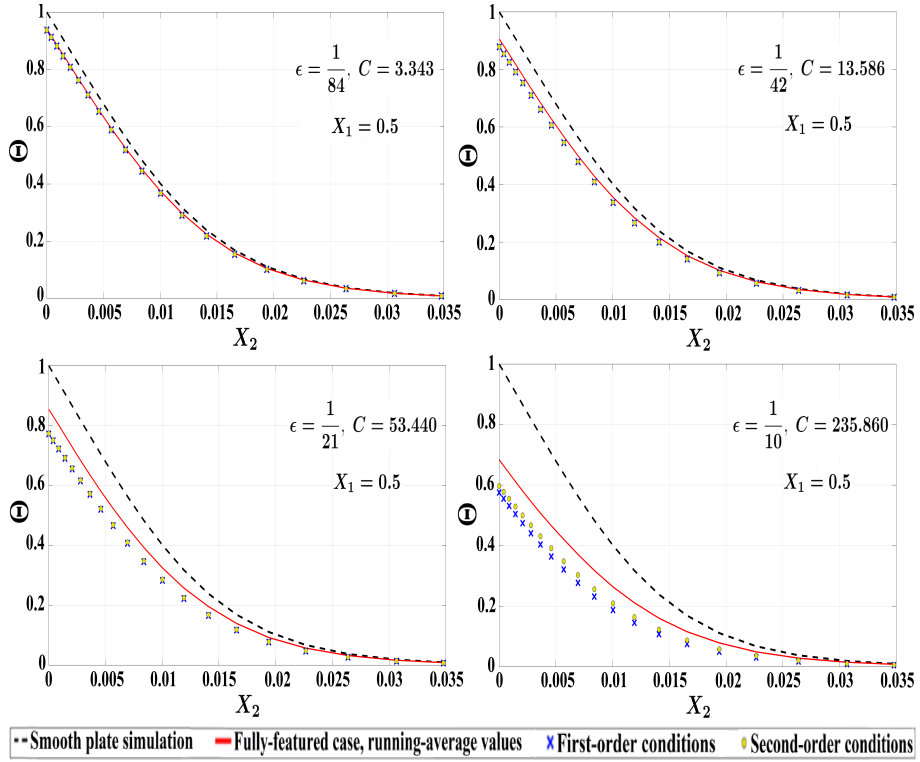


Figure 16: Predictions of the homogenized-models in comparison to the fully-featured running-average results of the dimensionless temperature profiles at  $X_1 = 0.5$  for different values of  $\epsilon$ .  $\frac{l}{\epsilon} = 3.75$ ,  $Gr = 5.563 \times 10^8$ ,  $Pr = 0.712$ .

The most important factor from the practical point of view is the surface-averaged Nusselt number. The behavior of  $\overline{Nu}$  with the increase of  $\epsilon$  is shown in Figure 17. It is obvious that the level of accuracy of the model predictions is even better than that relative to velocity and temperature profiles. It is also noteworthy that improved predictions of  $\overline{Nu}$  by shifting up to the second-order conditions are not systematically guaranteed.

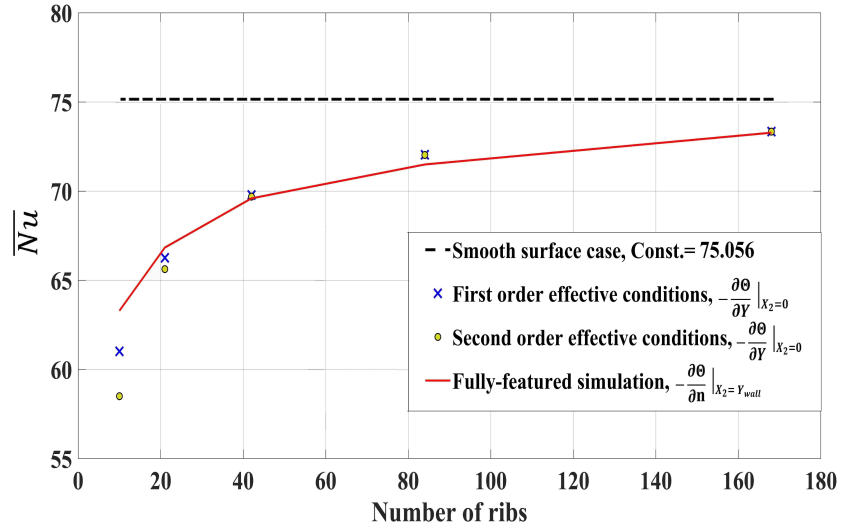


Figure 17: Effect of the number of the ribs ( $N_{ribs} = \frac{1}{\epsilon}$ ) on the surface-averaged Nusselt number (corrected to account for the increase in surface area in the case of feature-resolving simulations for the case of a ribbed surface, cf. Eq. (5-b)). The parameters are  $\frac{1}{\epsilon} = 3.75$ ,  $Gr = 5.563 \times 10^8$ ,  $Pr = 0.712$ .

The accuracy of the homogenization-based models is reported in a more quantitative manner in Table 1. For the velocity and temperature profiles shown in Figures 15 and 16, root-mean-square (rms) deviations between the results of the macroscopic simulations and the results of the reference fully-featured simulations are defined. The rms deviations of the profiles are calculated over a normal distance between  $X_2 = 0$  and  $X_2 = 0.02$ . For instance, the rms deviation of a modeled velocity profile ( $U_{mod}$  vs.  $X_2$ ) relative to the corresponding fully-featured one ( $U_{FF}$  vs.  $X_2$ ) is defined as

$$rms \ deviation = \sqrt{\frac{1}{0.02} \int_0^{0.02} \left( \frac{U_{mod} - U_{FF}}{U_{FF}} \right)^2 dX_2}. \quad (9)$$

The errors on the predictions of the surface-averaged Nusselt number relative to the fully-featured estimations are also shown in the table.

Table 1: Error estimations of the homogenized models predictions for the velocity and temperature profiles at  $X_1 = 0.5$  and surface-averaged Nusselt number. The fully-featured case is used as a reference. The deviations of the results of the smooth wall case compared to the rough case are also provided. In all cases:  $\frac{l}{e} = 3.75$ ,  $Gr = 5.563 \times 10^8$ ,  $Pr = 0.712$ .

		rms deviations of $U_1$ vs. $X_2$ profiles at $X_1=0.5$		
$\epsilon$	C	Smooth	First-order model	Second-order model
$\frac{1}{168}$	0.835	15.877%	1.491%	1.465%
$\frac{1}{84}$	3.340	17.312%	5.643%	5.420%
$\frac{1}{42}$	13.371	19.397%	13.473%	12.304%
$\frac{1}{21}$	53.485	22.566%	25.475%	20.076%
$\frac{1}{10}$	235.860	31.660%	56.025%	30.069%
		rms deviations of $\Theta$ vs. $X_2$ profiles at $X_1=0.5$		
$\epsilon$	C	Smooth	First-order model	Second-order model
$\frac{1}{168}$	0.835	3.044%	1.602%	1.617%
$\frac{1}{84}$	3.340	6.639%	1.909%	1.893%
$\frac{1}{42}$	13.371	11.689%	5.336%	5.220%
$\frac{1}{21}$	53.485	21.486%	12.781%	11.911%
$\frac{1}{10}$	235.860	49.687%	27.629%	19.887%
		relative error on $\overline{Nu}$		
$\epsilon$	C	Smooth	First-order model	Second-order model
$\frac{1}{168}$	0.835	2.529%	0.183%	0.181%
$\frac{1}{84}$	3.340	4.980%	0.759%	0.745%
$\frac{1}{42}$	13.371	7.846%	0.274%	0.139%
$\frac{1}{21}$	53.485	12.299%	-0.857%	-1.807%
$\frac{1}{10}$	235.860	18.580%	-3.605%	-7.575%

#### 4.2. Effect of the Grashof number at a given $\epsilon$

390 The observed deterioration of the predictions at relatively high values of  $\epsilon$  is not explicitly related to the increase in  $\epsilon$ ; rather, it is due to the associated increase of the convective coefficient  $C = \epsilon^2 \sqrt{Gr}$  beyond a critical limit which can be reached even at moderate/low values  $\epsilon$  when the Grashof number is large. In many instances [23, 24, 29], the theory has been validated for  $\epsilon$  up to 0.2.

395 Here, we set  $\epsilon = 0.1$  and show that by reducing the Grashof number (and thus,  $C$ ), the accuracy of the model improves. The macroscopic simulations are now set at a Grashof number of  $7.509 \times 10^6$  (instead of  $5.563 \times 10^8$ ), which results in a decrease of the convective coefficient  $C$  from 235.860 to 27.402. Figure 18 demonstrates that even at first order, the effective conditions provide a very

400 good match with fully-featured simulation results when  $C$  is reduced by one

order of magnitude. The same occurs for the temperature field (Figure 19) and the local Nusselt number (Figure 20).

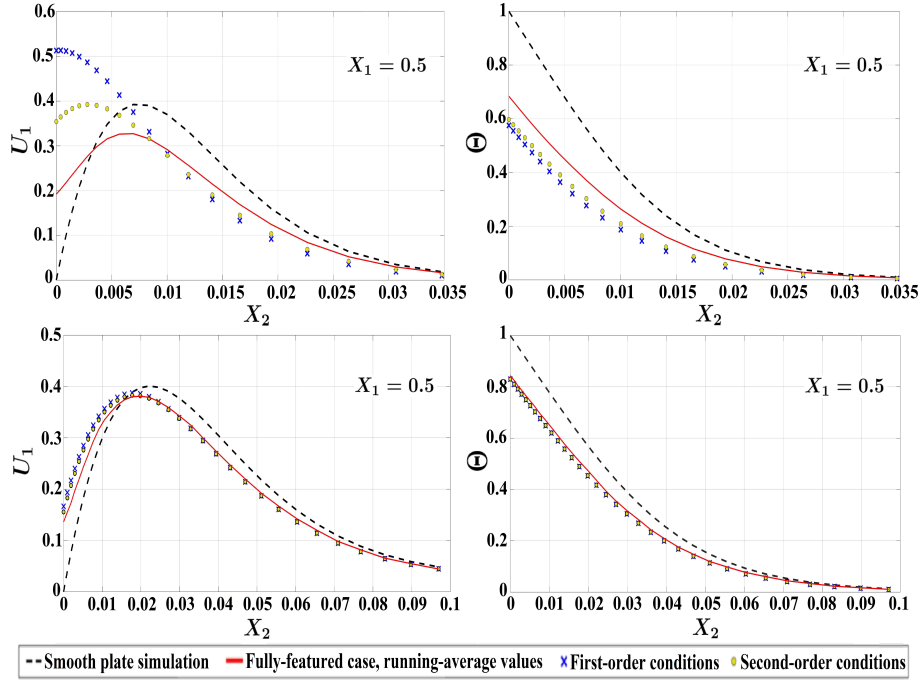


Figure 18: Predictions of the homogenized models in comparison to the fully-featured running-average results of the dimensionless streamwise velocity and temperature across a normal section at  $X_1 = 0.5$ , for two values of  $Gr$ : (top)  $Gr = 5.563 \times 10^8$ ; (bottom)  $Gr = 7.509 \times 10^6$ . For both cases,  $\epsilon = \frac{1}{10}$ ,  $\frac{l}{e} = 3.75$ ,  $Pr = 0.712$ .

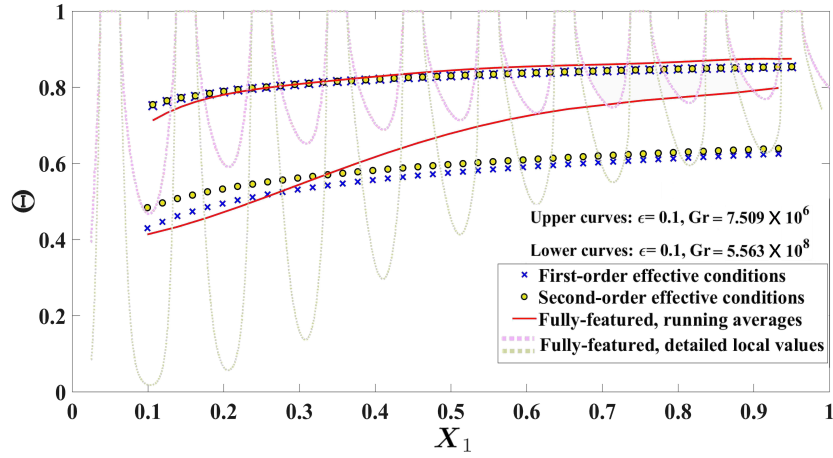


Figure 19: Predictions of the temperature behavior along the vertical fictitious surface ( $X_2 = 0$ ) at two values of  $Gr$ . In both cases:  $\epsilon = \frac{1}{10}$ ,  $\frac{l}{e} = 3.75$ ,  $Pr = 0.712$ .

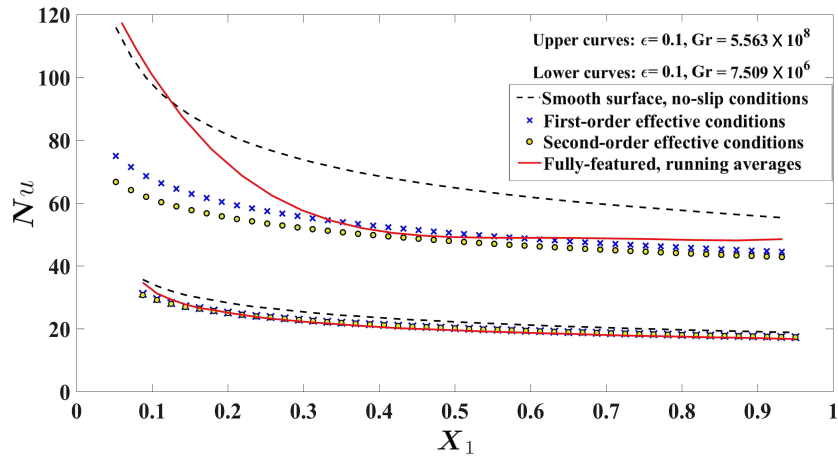


Figure 20: Predictions of the Nusselt number behavior at two values of  $Gr$ . In both cases:  $\epsilon = \frac{1}{10}$ ,  $\frac{l}{e} = 3.75$ ,  $Pr = 0.712$ .

## 5. Formal validity limit and final comments

### 5.1. Establishment of a formal validity limit

405 It has been argued in Section 4 that the accuracy of the proposed homogenization-based model may be linked to a single controlling parameter ( $C$ ) that combines the effects of  $\epsilon$  and  $Gr$  in the form  $C = \epsilon^2 \sqrt{Gr}$ . Therefore, it is advantageous to define a limiting value of  $C$  below which the predictions of the presented model

are assumed to be reliable. Based on analysis of the accuracy levels shown in  
 410 Table 1, the critical value of  $C$  is expected to be around 40; below this value,  
 rms deviations of the predicted velocity and temperature profiles are, respectively,  
 below 20% and 10%, and the absolute error on the predicted  $\overline{Nu}$  is less  
 than 1.5%, based on first-order and second-order accurate effective conditions.

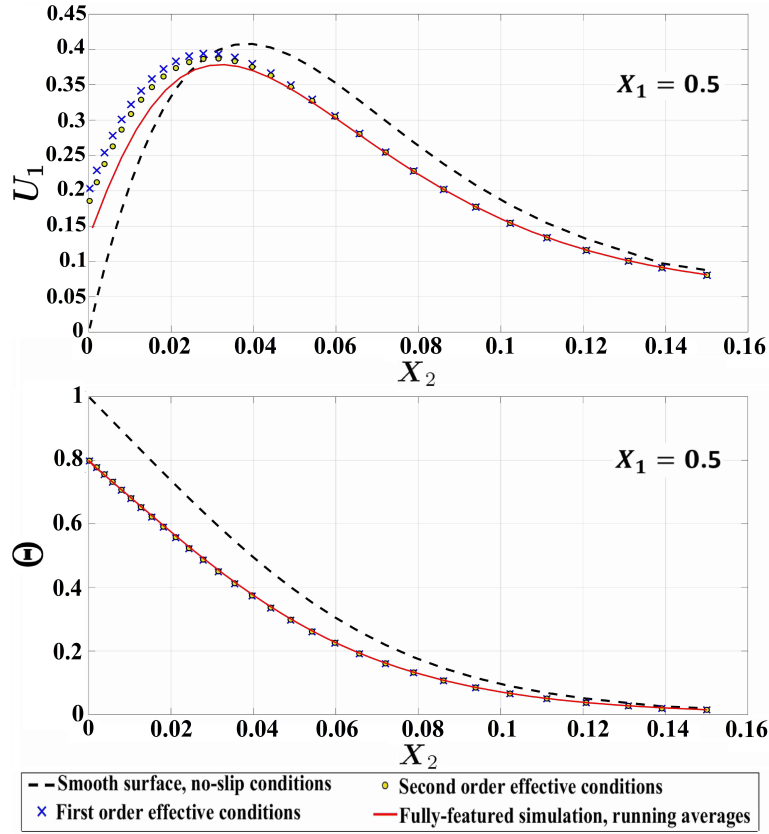


Figure 21: Predictions of the homogenized-models in comparison to the fully-featured running-average results of the dimensionless temperature profiles at  $X_1 = 0.5$ .  $\epsilon = 0.2$ ,  $\frac{l}{e} = 3.75$ ,  $Gr = 9.386 \times 10^5$ ,  $Pr = 0.712$ .

To validate this estimate, the simulation of the macroscopic problem has been  
 415 carried out for the case of a vertical surface roughened with only five square ribs,  
 i.e.  $\epsilon = 0.2$ , at  $Gr = 9.386 \times 10^5$  so that the accuracy of the model at a value of  
 $C = 38.752$  can be checked. The geometry of the ribs is characterized by a value  
 of  $\frac{l}{e} = 3.75$ ; the model coefficients given in Eq. (7) are used. The accuracy of

the model is assessed through comparative analysis of velocity and temperature  
 420 predictions across a normal section at  $X_1 = 0.5$  (Figure 21). Although the  
 velocity predictions in the near-wall region are not perfect, especially with the  
 first-order conditions, the temperature results are almost identical to the fully-  
 featured running-average behavior. From a practical point of view, the reliability  
 of the thermal field predictions is sufficient to consider the model acceptable  
 425 under the given condition, i.e.  $C \lesssim 40$ .

### 5.2. Conclusions and final comments

In this work, the natural convection over an isothermal vertical ribbed sur-  
 face has been considered. The homogenization-based effective conditions that  
 were established in Part 1 [26], without requiring any empirical input, have  
 430 been tested for the case of square ribs. The efficiency of the proposed first-  
 order and second-order accurate conditions in modeling the effect of the surface  
 microstructure on the macroscopic behavior of the flow has been tested by com-  
 paring the obtained thermal and velocity fields with the corresponding results of  
 the full feature-resolving simulations at different values of  $\epsilon = \frac{1}{N_{ribs}}$  and Grashof  
 435 number. All the simulations have been conducted for laminar flow conditions at  
 a constant Prandtl number equal to 0.712. It is shown that the expensive mesh  
 requirements for resolving complex inter-rib flow structures, associated with the  
*Separation-Reattachment-Separation* (SRS) regime at low values of  $Gr_x$  and the  
*Full Separation* (FS) regime at high values of  $Gr_x$ , can be significantly alleviated  
 440 when the model is employed. The most significant finding is that the accuracy  
 level of the model can be formally linked to the single parameter  $C = \epsilon^2 \sqrt{Gr}$   
 which measures the significance of the energy flux within the microscopic do-  
 main. A value of  $C \approx 40$  is estimated to be the critical limit below which the  
 model provides reasonable predictions.

445 The dependence of the accuracy of the proposed model on a single parameter  
 combining the effects of  $\epsilon$  and  $Gr$  renders the approach applicable to large values  
 of the Grashof number, provided that the value of  $\epsilon$  is sufficiently small, i.e.  
 the number of ribs is adequately large. The validated asymptotically upscaled

model in this work represents a more versatile version of the effective conditions  
450 to study natural convection over ribbed surfaces in comparison to the earlier  
model by Introïni et al. [30] who neglected the buoyancy effect in the microscopic  
region and reported a single validity-limiting value of  $Gr = 10^7$ . It should be  
noted that the reported limit of  $C \approx 40$  in this paper is related to the laminar  
flow regime only and does not guarantee the efficiency of the model in handling  
455 turbulent flows.

In pursuit of a more comprehensive understanding of the applicability limits  
of the model developed, along with its efficient use, the following activities are  
ongoing:

1. investigate the accuracy of the model for different shapes and dimensions  
460 of the ribs;
2. employ the approach to build and validate effective boundary conditions  
for the case of three-dimensional ribs;
3. study the performance and the accuracy limits of the model in the case of  
turbulent natural-convection flows over ribbed surfaces;
- 465 4. reconstruct the upscaled model to handle different thermal conditions of  
the surface, i.e. constant heat flux or adiabatic ribs;
5. establish a homogenization-based optimization technique through which  
the optimum surface structure can be sought for the maximization of the  
heat transfer from the surface under given constraints.

#### 470 **Acknowledgements**

The financial support of the Italian Ministry of University and Research, pro-  
gram PRIN 2017, project 2017X7Z8S3 LUBRI-SMOOTH, is gratefully acknowl-  
edged.

## References

- 475 [1] S. H. Bhavnani, A. E. Bergles, Effect of surface geometry and orientation  
on laminar natural convection heat transfer from a vertical flat plate with  
transverse roughness elements, *International Journal of Heat and Mass  
Transfer* 33 (5) (1990) 965–981. doi:10.1016/0017-9310(90)90078-9.
- [2] C. E. Johnson, Evaluation of correlations for natural convection cooling  
480 of electronic equipment, *Heat Transfer Engineering* 7 (1-2) (1986) 36–45.  
doi:10.1080/01457638608939643.
- [3] Y. Joshi, T. Willson, I. Hazard, S. J., An experimental study of natural  
convection from an array of heated protrusions on a vertical surface in  
water, *Journal of Electronic Packaging* 111 (2) (1989) 121–128. doi:10.  
485 1115/1.3226516.
- [4] R. S. Bunker, K. F. Donnellan, Heat transfer and friction factors for flows  
inside circular tubes with concavity surfaces, *J. Turbomach.* 125 (4) (2003)  
665–672. doi:10.1115/1.1622713.
- [5] M. Chyu, E. Oluyede, H.-K. Moon, Heat transfer on convective surfaces  
490 with pin-fins mounted in inclined angles, in: *Turbo Expo: Power for Land,  
Sea, and Air*, Vol. 47934, 2007, pp. 861–869. doi:10.1115/GT2007-28138.
- [6] J.-C. Han, S. Dutta, S. Ekkad, *Gas Turbine Heat Transfer and Cooling  
Technology*, CRC Press, 2012.
- [7] G. Tanda, Natural convection heat transfer in vertical channels with and  
495 without transverse square ribs, *International Journal of Heat and Mass  
Transfer* 40 (9) (1997) 2173–2185. doi:10.1016/S0017-9310(96)00246-3.
- [8] M. Aydin, Dependence of the natural convection over a vertical flat plate in  
the presence of the ribs, *International Communications in Heat and Mass  
Transfer* 24 (4) (1997) 521–531. doi:10.1016/S0735-1933(97)00037-7.

- 500 [9] S. Onbaşıoğlu, A. Egrİcan, Enhancement of heat transfer with horizontal promoters, in: *Heat Transfer Enhancement of Heat Exchangers*, Springer, 1999, pp. 433–446.
- [10] M. Nishikawa, H. Otomo, Y. Yoshida, J. Deguchi, M. Tsukamoto, T. Yamamoto, The cooling mechanism of minuscule ribbed surfaces, *Scientific Reports* 10 (1) (2020) 1–6.
- 505 [11] G. Tanda, Natural convective heat transfer in vertical channels with low-thermal-conductivity ribs, *International Journal of Heat and Fluid Flow* 29 (5) (2008) 1319–1325. doi:10.1016/j.ijheatfluidflow.2008.05.004.
- 510 [12] M. Cavazzuti, M. A. Corticelli, Optimization of a buoyancy chimney with a heated ribbed wall, *Heat and Mass Transfer* 44 (4) (2008) 421–435. doi:10.1007/s00231-007-0255-6.
- [13] S. Bhavnani, A. Bergles, Natural convection heat transfer from sinusoidal wavy surfaces, *Wärme-und Stoffübertragung* 26 (6) (1991) 341–349.
- 515 [14] L.-S. Yao, Natural convection along a vertical complex wavy surface, *International Journal of Heat and Mass Transfer* 49 (1-2) (2006) 281–286. doi:10.1016/j.ijheatmasstransfer.2005.06.026.
- [15] K. Kishinami, H. Saito, I. Tokura, An experimental study on natural convective heat transfer from a vertical wavy surface heated at convex/concave elements, *Experimental Thermal and Fluid Science* 3 (3) (1990) 305–315.
- 520 doi:10.1016/0894-1777(90)90005-R.
- [16] J. Hærvig, H. Sørensen, Natural convective flow and heat transfer on unconfined isothermal zigzag-shaped ribbed vertical surfaces, *International Communications in Heat and Mass Transfer* 119 (2020) 104982. doi:10.1016/j.icheatmasstransfer.2020.104982.
- 525 [17] I. El Ghandouri, A. El Maakoul, S. Saadeddine, M. Meziane, Design and numerical investigations of natural convection heat transfer of a new rip-

- pling fin shape, *Applied Thermal Engineering* 178 (2020) 115670. doi:10.1016/j.applthermaleng.2020.115670.
- 530 [18] G. Guglielmini, E. Nannei, G. Tanda, Natural convection and radiation heat transfer from staggered vertical fins, *International Journal of Heat and Mass Transfer* 30 (9) (1987) 1941–1948. doi:10.1016/0017-9310(87)90252-3.
- [19] M. Ahmadi, G. Mostafavi, M. Bahrami, Natural convection from rectangular interrupted fins, *International Journal of Thermal Sciences* 82 (2014) 62–71. doi:10.1016/j.ijthermalsci.2014.03.016.
- 535 [20] M. Imbriale, M. Panelli, G. Cardone, Heat transfer enhancement of natural convection with ribs, *Quantitative InfraRed Thermography Journal* 9 (1) (2012) 55–67. doi:10.1080/17686733.2012.681881.
- [21] G. Tanda, Experiments on natural convection in water-cooled ribbed channels with different aspect ratios, *International Journal of Heat and Mass Transfer* 110 (2017) 606–612. doi:10.1016/j.ijheatmasstransfer.2017.03.050.
- 540 [22] S. Jiménez Bolaños, B. Vernescu, Derivation of the Navier slip and slip length for viscous flows over a rough boundary, *Physics of Fluids* 29 (5) (2017) 057103. doi:10.1063/1.4982899.
- [23] U. Lācis, Y. Sudhakar, S. Pasche, S. Bagheri, Transfer of mass and momentum at rough and porous surfaces, *Journal of Fluid Mechanics* 884 (2020) A21. doi:10.1017/jfm.2019.897.
- 550 [24] A. Bottaro, S. B. Naqvi, Effective boundary conditions at a rough wall: a high-order homogenization approach, *Meccanica* 55 (9) (2020) 1781–1800. doi:10.1007/s11012-020-01205-2.
- [25] G. A. Ledezma, A. Bejan, Optimal geometric arrangement of staggered vertical plates in natural convection, *Journal of Heat Transfer* 119 (4) (1997) 700–708. doi:10.1115/1.2824174.
- 555

- [26] E. N. Ahmed, A. Bottaro, G. Tanda, Natural convection along a micro-patterned vertical wall. Part 1: A multiscale homogenization approach to establish *effective* boundary conditions, International Journal of Heat and Mass Transfer. Submitted (2021).
- 560 [27] J. H. Lienhard IV, J. H. Lienhard V, A Heat Transfer Textbook, 5th edn, Phlogiston Press, 2019.
- [28] S. Ostrach, An analysis of laminar free-convection flow and heat transfer about a flat plate parallel to the direction of the generation body force, NACA Technical Report 1111 (1953).
- 565 [29] A. Bottaro, Flow over natural or engineered surfaces: an adjoint homogenization perspective, Journal of Fluid Mechanics 877 (2019) P1. doi:10.1017/jfm.2019.607.
- [30] C. Introïni, M. Quintard, F. Duval, Effective surface modeling for momentum and heat transfer over rough surfaces: application to a natural convection problem, International Journal of Heat and Mass Transfer 54 (15-16)  
570 (2011) 3622–3641. doi:10.1016/j.ijheatmasstransfer.2011.03.019.